The Astrophysical Journal, 937:41 (12pp), 2022 September 20 https://doi.org/10.3847/1538-4357/ac8870

Spatial Scales and Time Variation of Solar Subsurface Convection

Alexander V. Getling[1] and Alexander G. Kosovichev[2]
[1] Skobeltsyn Institute of Nuclear Physics, Lomonosov Moscow State University, Moscow, 119991, Russia; A.Getling@mail.ru
[2] New Jersey Institute of Technology, Newark, NJ 07102, USA
Received 2022 May 17; revised 2022 August 5; accepted 2022 August 8; published 2022 September 26

Abstract

Spectral analysis of the spatial structure of solar subphotospheric convection is carried out for subsurface flow maps constructed using the time–distance helioseismological technique. The source data are obtained from the Helioseismic and Magnetic Imager on board the Solar Dynamics Observatory from 2010 May to 2020 September. A spherical harmonic transform is applied to the horizontal velocity divergence field at depths from 0 to 19 Mm. The range of flow scales is fairly broad in the shallow layers and narrows as the depth increases. The horizontal flow scales increase rapidly with depth, from supergranulation to giant-cell values, and indicate the existence of large-scale convective motions in the near-surface shear layer. The results can naturally be interpreted in terms of a superposition of differently scaled flows localized at different depth intervals. There is some tendency toward the emergence of meridionally elongated (banana-shaped) convection structures in the deep layers. The total power of the convective flows is anticorrelated with the sunspot number variation over the solar activity cycle in shallow subsurface layers, and positively correlated at larger depths, which is suggestive of the depth redistribution of the convective flow energy due to the action of magnetic fields.

Unified Astronomy Thesaurus concepts: Helioseismology (709); Solar granulation (1498); Solar activity (1475)

1. Introduction

As is known, plasma flows in the solar convection zone form variously scaled structures resembling convection cells. The smallest of them, granules, have been known since the advent of high-resolution telescopic observations of the Sun (Herschel 1800). Frenkiel & Schwarzschild (1952) performed the first analysis of the turbulence spectrum of solar convection and, in addition to the primary maximum corresponding to granulation, found a secondary maximum at long wavelengths corresponding to 15 Mm. Based on Doppler measurements of horizontal velocities (away from the disk center), Hart (1954) discovered signs of a pattern of cells with sizes an order of magnitude larger and living much longer than granules. Leighton et al. (1962) described them in greater detail and designated them as supergranules. For a recent review of studies of supergranulation, see Rincon & Rieutord (2018). Further, November et al. (1981), using Doppler measurements of vertical velocities, detected mesogranulation—a system of cells intermediate between granules and supergranules in their sizes. The existence of the largest velocity field structures, giant cells, was suggested long ago by Simon & Weiss (1968). Even before that, Bumba et al. (1964) noted indications of the presence of giant structures when observing magnetic fields. However, giant cells were qualified to be hypothetical for more than three decades.

Glatzmaier & Gilman (1981) performed a linear analysis of the onset of convection in a rotating spherical shell using the anelastic approximation. They found that giant cells extending from the bottom to the top of the convection zone are the most easily excitable instability mode. As the density stratification and rotation rates increase, these cells become meridionally elongated, or banana-shaped. Possibilities of banana-shaped cells have been repeatedly noted since the early 1970s (Busse 1970); see also a survey by Busse (2002). In particular, such cells were demonstrated in laboratory experiments (Busse & Carrigan 1974). Giant cellular structures were also found in global magnetohydrodynamic simulations of the solar convection zone dynamo action (Ghizaru et al. 2010). Featherstone & Hindman (2016) simulated convection in the anelastic approximation using a spectral technique. They claimed that "the supergranular scale emerges due to a suppression of power on larger spatial scales owing to the presence of deep, rotationally constrained convection" and that "giant cells in the traditional sense do not exist."

The earliest direct Doppler observations of giant cells were done by Beck et al. (1998). Later, Hathaway et al. (2013) revealed them using supergranules as tracers of the material flow.

Lastly, Abramenko et al. (2012) reported the detection of mini-granules, whose sizes vary extremely widely. These features still remain very poorly studied.

The multiscale structure of solar convection raises some questions that can only be resolved using information about the velocity field in the subphotospheric convection zone. In particular, hydrodynamic considerations (see, e.g., Shcheritsa et al. 2018), along with the fact that smaller-scale convection cells are advected at the photospheric surface by the flows in larger-scale cells, and can be considered tracers of the large-scale velocity field (see, e.g., Muller et al. 1992; Rieutord et al. 2001; Getling & Buchnev 2010; Hathaway & Upton 2021), suggest that the convective velocity field represents a superposition of differently scaled flows (Getling & Buchnev 2010), in contrast to the idea of the mixing-length theory, that the flows have unique characteristic scales gradually increasing with depth. The progress of helioseismological research has made it possible to trace the structure and temporal evolution of the subsurface flow field.

The flow scales are characterized by the spatial spectra of the velocity field. In particular, Hathaway (1987) applied a

spherical harmonic transform to the photospheric Doppler velocity signal and investigated the spatial scales of supergranules and giant cells. Hathaway et al. (2000, 2015) continued this line of research. They noted the broadband nature of the convection spectrum and employed a data-filtering technique to isolate the granular and the supergranular scales. Greer et al. (2015) employed ring-diagram techniques to study the strength and spatial scale of convective flows in the near-surface shear layer. In particular, they found that the peak of the horizontal velocity spectrum shifts with depth from higher to smaller values of the spherical harmonic degree.

The spectral composition of the velocity spectrum at various depths below the photosphere has not yet received sufficient attention. We aim to study the spatiotemporal structure of subphotospheric convection using the full-disk horizontal velocity maps obtained from the Helioseismic and Magnetic Imager (HMI; Scherrer et al. 2012) on board the Solar Dynamics Observatory, and available from the Joint Science Operations Center.[3] In particular, we construct the spatial spectra of the horizontal velocity fields in the depth range from 0 to 19 Mm, obtained from the time–distance helioseismology pipeline, and analyze the variations of the spectra with depth and time in the course of the solar activity cycle. These data resolve the supergranulation and convective flows of larger scales.

Attempts to investigate variations in the convection patterns over the activity cycle are not numerous (see, in particular, the references in Roudier & Reardon 1998 and Muller et al. 2018). Lefebvre et al. (2008) found that the granulation evolves with height in the photosphere, but does not exhibit considerable variations in the activity cycle. In addition, McIntosh et al. (2011) studied the variation of the supergranular length scale over multiple solar minima. Muller et al. (2018) detected no significant variations in the granulation scale with the activity cycle. Ballot et al. (2021) have shown that the densities and the mean areas of granules experience an approximately 2% variation over the course of the solar cycle, the density of the granules being greater and the area being smaller at the solar maximum.

In this paper, we show that the subsurface flow represents a superposition of multiscale convective structures traced at various levels in the upper convection zone. In particular, the scale of giant cells is present in the velocity spectrum, along with the supergranulation scales. In addition, we demonstrate variations of the integrated power of the velocity field over the course of the solar cycle.

2. The Data and Processing Techniques Used

The original subsurface flow maps for the central $123^\circ \times 123^\circ$ area of the visible hemisphere of the Sun are routinely produced every 8 hr by the time–distance helioseismology pipeline (Zhao et al. 2012b) from the HMI Dopplergrams. They are represented on a grid of 1026×1026 points, with a spatial sampling interval of $0\overset{\circ}{.}12$ in both longitude and latitude. We use the data for the horizontal velocities at the following eight characteristic levels below the photosphere (the corresponding depth ranges for which the inversions were done are parenthesized): $d = 0.5$ (0–1) Mm, 2.0 (1–3) Mm, 4.0 (3–5) Mm, 6.0 (5–7) Mm, 8.5 (7–10) Mm, 11.5 (10–13) Mm, 15.0 (13–17) Mm, and 19.0 (17–21) Mm. The travel-time measurements are described by Couvidat et al. (2012). The travel-time inversion procedure employed in the HMI pipeline uses Born approximation sensitivity kernels and provides a good localization of the averaging kernels at the target depth. However, the vertical width of the averaging kernels increases with depth, from ~2 Mm near the surface to ~10 Mm at the bottom layer (Couvidat et al. 2005, Figures 10 and 11). The horizontal width of the averaging kernels also increases with depth, from ~16 to ~40 Mm (Couvidat et al. 2005, Figures 11 and 12). Therefore, the flow maps represent the velocities convolved with the averaging kernels, and this should be taken into account in the interpretation of the presented results. To assess the possible effect of the averaging kernel variation with depth, we present an illustrative example in Section 3.2.

2.1. Spectral Representations

For convenience, we analyze the scalar field of the horizontal velocity divergence, rather than the velocity vector field, $\boldsymbol{V}$. On a sphere of radius r, the divergence of the vector $\boldsymbol{V} = \{V_\theta, V_\varphi\}$ is

$$f(\theta, \varphi) = \operatorname{div} \boldsymbol{V}(\theta, \varphi) = \frac{1}{r \sin\theta} \frac{\partial}{\partial\theta}(V_\theta \sin\theta) + \frac{1}{r \sin\theta} \frac{\partial}{\partial\varphi} V_\varphi, \quad (1)$$

where θ and φ are the polar and azimuthal angles and r merely plays the role of a parameter. We represent the divergence field as a polynomial expansion,

$$f(\theta, \varphi) = \sum_{l=0}^{l_{\max}} \sum_{m=-l}^{l} A_{lm} Y_l^m(\theta, \varphi), \quad (2)$$

in spherical harmonics of angular degree l and azimuthal order m,

$$Y_l^m = \sqrt{\frac{(2l+1)}{4\pi} \frac{(l-m)!}{(l+m)!}} P_l^m(\cos\theta) e^{im\varphi}, \quad l = 0,\ldots,l_{\max}, \quad m = 0,\ldots,l \quad (3)$$

where P_l^m are the associated Legendre polynomials and $l_{\max}$ is a properly chosen upper spectral boundary. The spectral coefficients (amplitudes of harmonics) can be determined in a standard way by the equation

$$A_{lm} = \frac{1}{4\pi} \int_0^\pi \int_0^{2\pi} f(\theta, \varphi) Y_l^m(\theta, \varphi) \sin\theta \, \mathrm{d}\varphi \, \mathrm{d}\theta. \quad (4)$$

We are interested here in the power spectra of the flow,

$$p_{lm} = |A_{lm}|^2. \quad (5)$$

According to Parseval's theorem, the integrated power of the flow represented by the spectrum (2) is

$$p_{\mathrm{tot}} \equiv \int_\Omega f^2 \, \mathrm{d}\Omega = \sum_{l=0}^{\infty} \sum_{m=-l}^{l} |A_{lm}|^2. \quad (6)$$

The normalized interior sum,

$$p_l = \frac{1}{2l+1} \sum_{m=-l}^{l} |A_{lm}|^2, \quad (7)$$

is, by definition, the power per degree l and per steradian (see, e.g., Equations (B.94) and (B.95) on page 858 in Dahlen & Tromp 1998). Such a normalization is chosen because it

[3] http://jsoc.stanford.edu/data/timed/

ensures a "flat" spectral representation, $p_l = 1/4\pi$, of a Dirac delta function on the unit sphere, $(\sin\theta)^{-1}\ \delta(\theta - \theta')\delta(\varphi - \varphi')$. In addition, we consider the total power of degree l,

$$p_l^{\Sigma} = \sum_{m=-l}^{l} |A_{lm}|^2. \tag{8}$$

To reduce the possible effects of short-term temporal fluctuations of the velocity field, we apply a running average procedure with a 45 day window to the power spectra, p_{lm}, and to the power functions, p_l and p_l^{Σ}.

Our source data do not cover the whole spherical surface. For this reason, we cut a longitudinal sector 120° wide out of each flow map and complement it with the same data, shifted by 120° and 240°, to fill the complete longitudinal angle. The resultant spectra thus contain nonzero harmonics only, with any m multiple of 3; we interpolate them to all missing m values and smooth the spectra with a two-point window for better visual perceptibility.

Since our source data are restricted to a latitudinal range of $\pm 61\overset{\circ}{.}5$, we have to investigate the effect of the "empty" polar caps on the spectrum. To this end, we apply our spectral analysis to a sample model velocity field obtained by G. Guerrero and A. M. Stejko using numerical simulations (2021, private communication), and compare the spectra obtained with and without artificially introduced zero velocity in the polar caps $-90° < \varphi < -61\overset{\circ}{.}5$ and $61\overset{\circ}{.}5 < \varphi < 90°$. In addition, we introduce a latitudinal tapering of the flow fields to reduce possible spurious effects due to the Gibbs phenomenon. In other words, we multiply the divergence fields by a window function, which smooths the sharp drop of velocities at latitudes of $\pm\, 61\overset{\circ}{.}5$—the boundaries of the "empty" polar caps. The analysis of the simulations shows that the "empty" polar caps only result in a moderate narrowing of the spectral l band. The latitudinal tapering also results in minimal changes in the flow spectrum.

According to the Jeans (1923) formula, the full wavelength of the harmonic Y_l^m on a sphere of radius r is

$$\lambda = \frac{2\pi r}{\sqrt{l(l+1)}} \tag{9}$$

(the layer that we consider is much thinner than the convection zone, and r can be put equal to the radius of the Sun, $R_\odot$). This wavelength, determined by the angular degree, l, of the spherical harmonic Y_l^m, can be used to estimate the characteristic size of the flow structures corresponding to this harmonic (Figure 1).

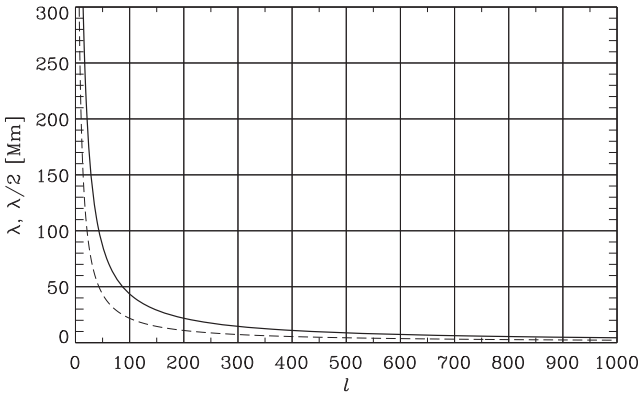

Figure 1. The full wavelength, λ, of the spherical harmonic Y_l^m and $\lambda/2$ for $r = R_\odot$, as determined by the Jeans formula (9).

3. Results

3.1. Unsmoothed Fields. Realization Noise

A visual inspection of the velocity divergence maps suggests that the characteristic scale of the convection flows increases with depth (Figure 2). The regularities of the depth variation of the flow scales are among the principal aims of our study. We start by describing the results for the fields whose spectral representations contain harmonics of orders $l \leqslant l_{\max} = 1000$. Therefore, the shortest wavelengths present in the spectra are about 2–4 Mm, which exceed the spatial sampling interval, or the pixel size of the maps, 1.46 Mm.

Due to the stochastic excitation of solar acoustic oscillations and their finite wavelength, the flow maps contain so-called "realization noise" (Gizon & Birch 2004), the spatial scale of which increases with depth. This scale can be estimated as the horizontal wavelength (or the corresponding angular degree, l) of acoustic waves at the inner turning point, where the wave phase speed, λ/T, is equal to the local sound speed, c (here, λ is the horizontal wavelength and T is the period of the wave). If λ is determined by Equation (9) and c is calculated from the standard solar model (see Christensen-Dalsgaard et al. 1996), then, for a frequency of $1/T \sim 3 \times 10^{-3}$ Hz, the dependence of the angular degree on the turning point depth appears as shown in Figure 3. It indicates that the scale of the realization noise due to 5 minute oscillations varies from $l \sim 1000$ in the top layers to $l \sim 250$ at depths of about 20 Mm. Higher-frequency waves have correspondingly shorter wavelengths. The l values plotted in Figure 3 can thus be used as an estimate for the long-wavelength bound of the realization noise.

Figure 4 shows the power spectra of the divergence field computed for all the eight depths and averaged over a 45 day time interval from 2019 December 21 to 2020 February 4, when the solar activity was low. The long-wavelength bound of the realization noise is marked with the red vertical lines in these spectra. Noise patterns can clearly be seen to the right of the red lines in the panels for $d \geqslant 6$ Mm. The left-hand parts of the diagrams represent the spectra of convective flows.

The flow maps used here have a pixel size of 1.46 Mm and do not resolve granulation. Supergranulation in the upper layers, $d = 0.5$–4 Mm, is mainly manifest in a degree range of $l \sim 70$–150, which corresponds to $\lambda \sim 30$–60 Mm. In the depth range of 6–11.5 Mm, a second spectral peak at $l \sim 150$–270, corresponding to a characteristic scale of $\lambda \sim 20$–30 Mm, emerges. It may be related to changes in the properties of supergranulation in these layers.

In the deep layers, harmonics with $l \sim 20$–30, of giant-cell scales $\lambda \sim 150$–200 Mm, are prominent. In the context of our particular interest in the steady, large-scale component of the spectrum, we can regard the rapidly changing convection as a noise component, along with the realization noise in the helioseismic measurements due to the stochastic excitation of solar oscillations. For this reason, from here on, we will consider spectra with this noise filtered out by a smoothing procedure.

3.2. Smoothed Fields. Flow Scales

We smooth the velocity field with a 17.5 Mm window and assume the upper spectral boundary in our analysis to be

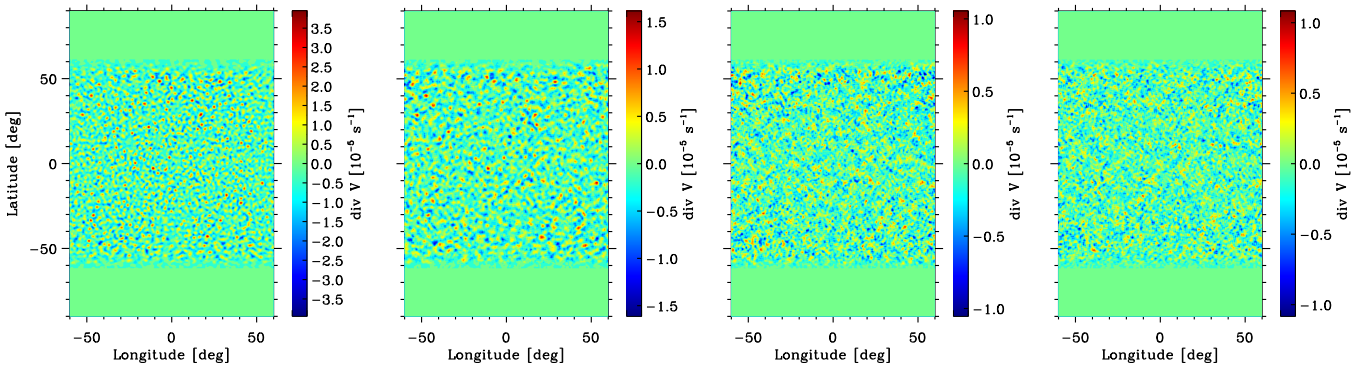

Figure 2. Sample maps of the divergence field at levels $d = 0.5$, 4.0, 6.0, and 11.5 Mm (from left to right), at the same time.

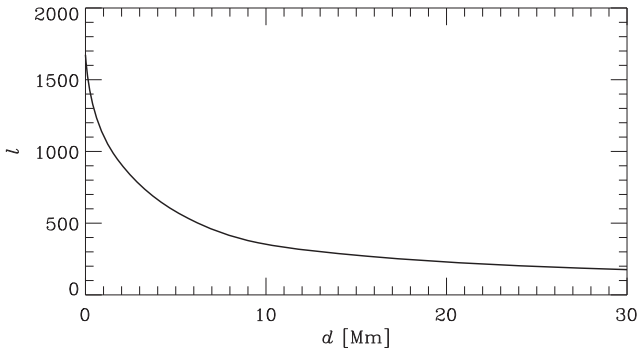

Figure 3. Estimated long-wavelength bound of the realization noise for an acoustic frequency of 3×10^{-3} Hz as a function of depth.

$l_{\max} = 200$. The depth variations of the power spectra of the smoothed convective flows is illustrated in Figure 5 for the same 45 day average interval as in Figure 4. The range of degrees l and the corresponding range of scales λ are fairly wide in the shallow layers. As d increases, the main spectral peak narrows and shifts into the low-l (long-wavelength) region. Although the long-wavelength part of the smoothed spectra (Figure 5) for deep layers visually appears to be more extended and more powerful than that of the unsmoothed ones (Figure 4), the power values and the peak widths are similar in both cases.

Such behavior of the spectra can naturally be explained in terms of a superposition of differently scaled flows: we will see that the supergranular-scale flows in the upper layers ($l \sim 70$–130, $\lambda \sim 30$–60 Mm) coexist with the upper parts of giant convection cells; they are much less manifest at the deep levels, where the largest-scale energetic harmonics have $l \sim 10$ and the corresponding wavelength range is broad and centered at 300 Mm—a giant-cell scale. These scales, being pronounced in the bottom half of the considered layer, are not so noticeable near the surface, because the color scale used for the graphic representation of the spectra is determined by the more energetic, smaller-scale flows. However, the power values for the largest scales at the upper and deep levels are comparable—we discuss this fact below, by considering the depth (d-) variation of the m-averaged power spectrum defined by Equation (7), p_l, as a function of l.

Spectra obtained for a period of high solar activity, 2013 December 18–2014 February 1, are presented in Figure 6. Visually, they are very similar to those in Figure 5. The differences between the two cases are mainly in the extremum power values, rather than in the shapes of the spectra. We discuss the effects of the solar activity level in Section 3.3.

Figure 7 shows the m-averaged spectra, p_l, obtained from the original spectra displayed in Figure 5. The uncertainty of the results is calculated as the standard deviation of the power p_l from its running average, and indicated by dotted curves. The total powers of the harmonics with a given l, calculated according to Equation (8), p_l^{Σ}, are also shown in Figure 7, with the dashed curves.

Let us compare the p_l values for the largest-scale harmonics at different depths. The p_l spectra demonstrate the displacement of the main peak to longer wavelengths with depth. The peak of the spectrum for $d = 19$ Mm is near $l \approx 13$, and its height is about 8.5×10^{-9} s^{-2}. At $d = 0.5$ Mm, the power values for such wavenumbers are about 5×10^{-9} s^{-2}. Similar p_l values in this long-wavelength range are also typical of the intermediate depths. Therefore, the flows characterized by the horizontal scales in the range $\lambda \sim 200$–300 Mm have comparable power values over the whole depth range. However, near the surface, the supergranulation-scale flows are much more powerful than the large-scale flows. The spectrum thus represents a superposition of flow components with widely differing scales: the supergranular-scale components are dominant in the upper layers, while the weaker larger-scale components extend from deep to shallow layers.

The helioseismic inferences yield estimates of the flow velocities averaged with kernels of characteristic widths increasing with depth. To evaluate the possible effect of the averaging kernel broadening with depth, we computed the p_l spectra of a convective velocity divergence field for $d = 0.5$ Mm, smoothed with Gaussian kernels whose widths vary over the same range as the kernels used in helioseismological inversions (Couvidat et al. 2005). The p_l spectra corresponding to the extreme kernel width values, $w = 17$ and 38 Mm, are displayed in the bottom right panel of Figure 7, and demonstrate only a moderate shift of the spectrum to longer wavelengths with depth, which does not affect our conclusions. Small near-surface sidelobes of the averaging kernels might, in principle, contribute to the power enhancement at small scales in the deep layers. However, this is unlikely, since the sidelobes in both the vertical and horizontal directions are fairly weak compared to the primary averaging kernel peak (Couvidat et al. 2005, Figure 11).

It is worth noting one more particular feature of the spectra shown in Figure 5. Since the harmonics for $l = m$ are sectorial (latitude-independent), the fact that the main spectral peak approaches the $l = m$ line with the increase of d can be interpreted as an indirect indication of the presence of meridionally elongated, banana-shaped convection structures.

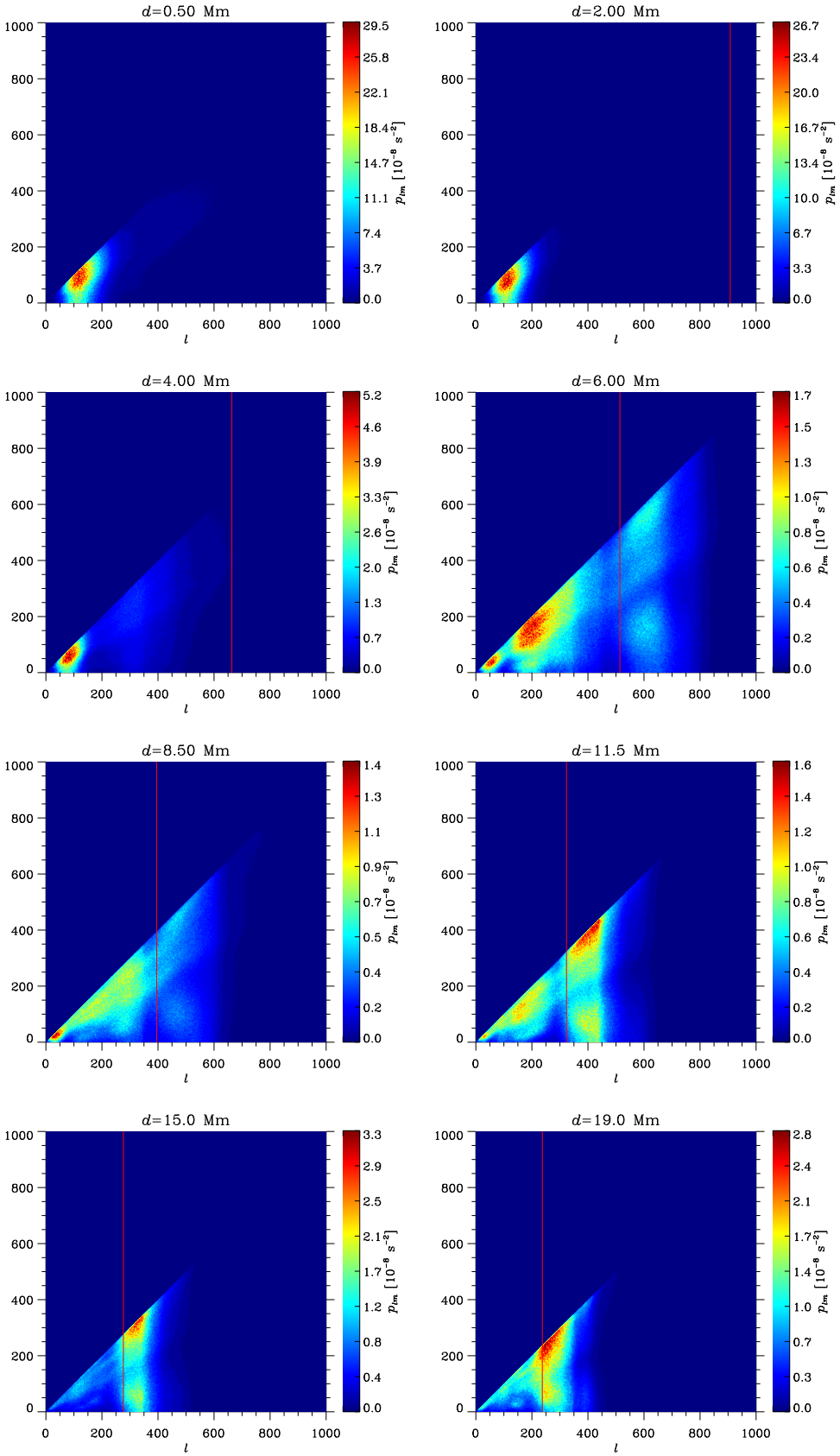

Figure 4. Depth variations of sample power spectra of the divergence of the unsmoothed velocity field, p_{lm}, with $l_{\max} = 1000$ obtained by 45 day averaging over the low-activity period from 2019 December 21 to 2020 February 4. The red vertical line in each spectrum marks the estimated long-wavelength spectral bound of the realization noise (Figure 3). The depth values are indicated at the top of each panel.

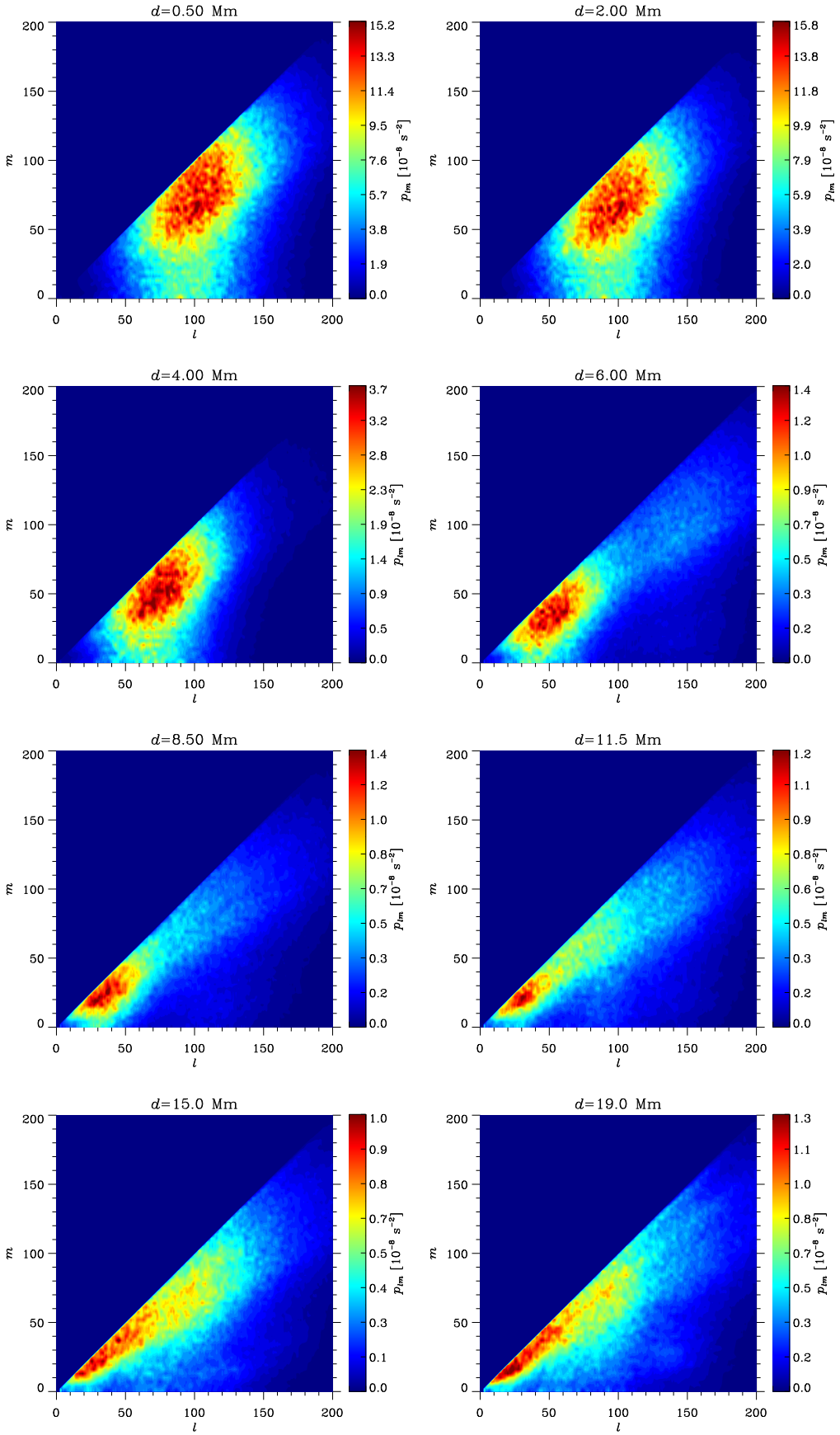

Figure 5. Depth variations of sample power spectra of the divergence of the velocity field smoothed with a 17.5 Mm window, p_{lm}, with $l_{\max} = 200$, obtained by 45 day averaging over the low-activity period from 2019 December 21 to 2020 February 4. The depth values are indicated at the top of each panel.

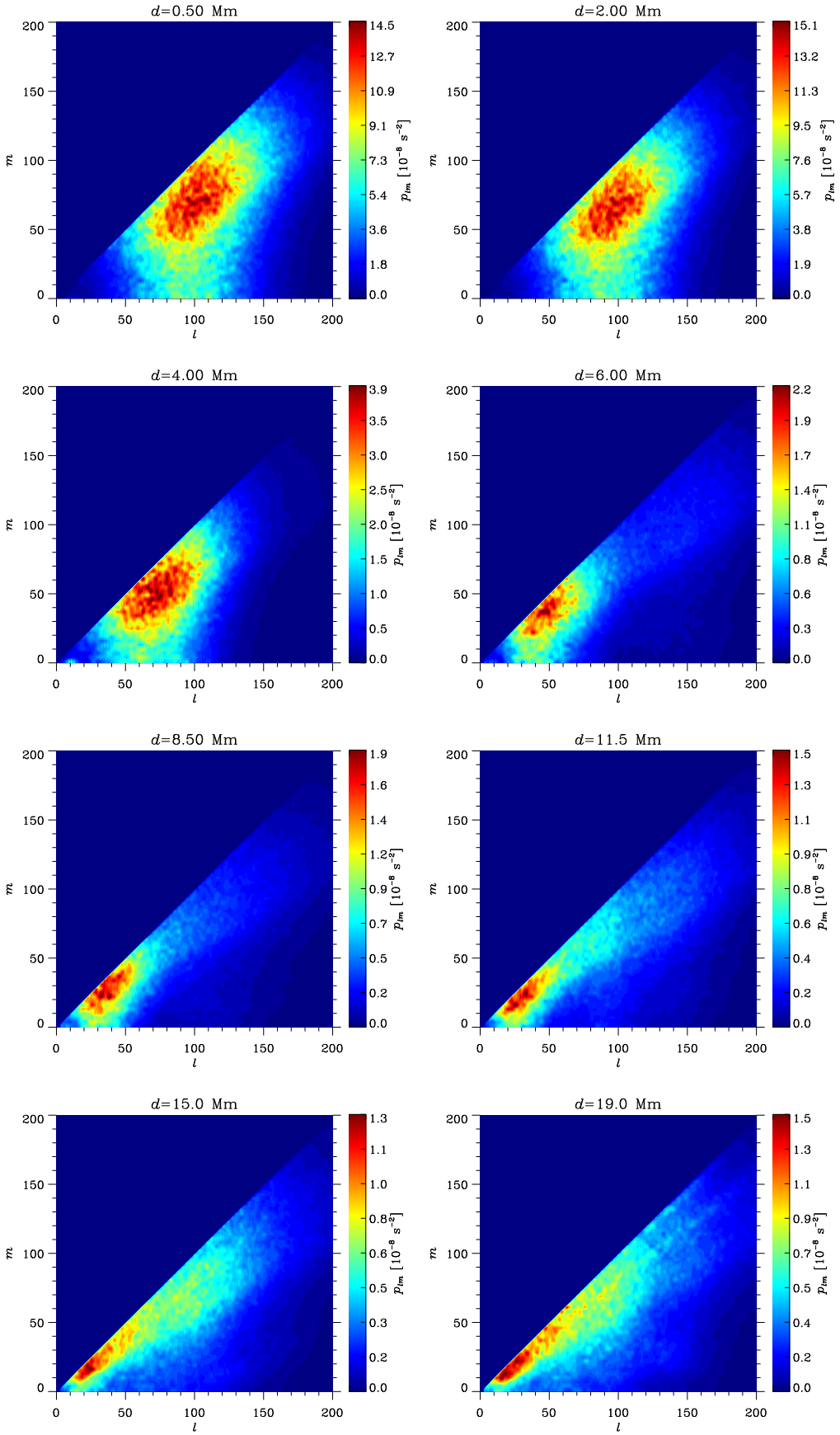

Figure 6. The same as Figure 5, but for the high-activity period from 2013 December 18 to 2014 February 1.

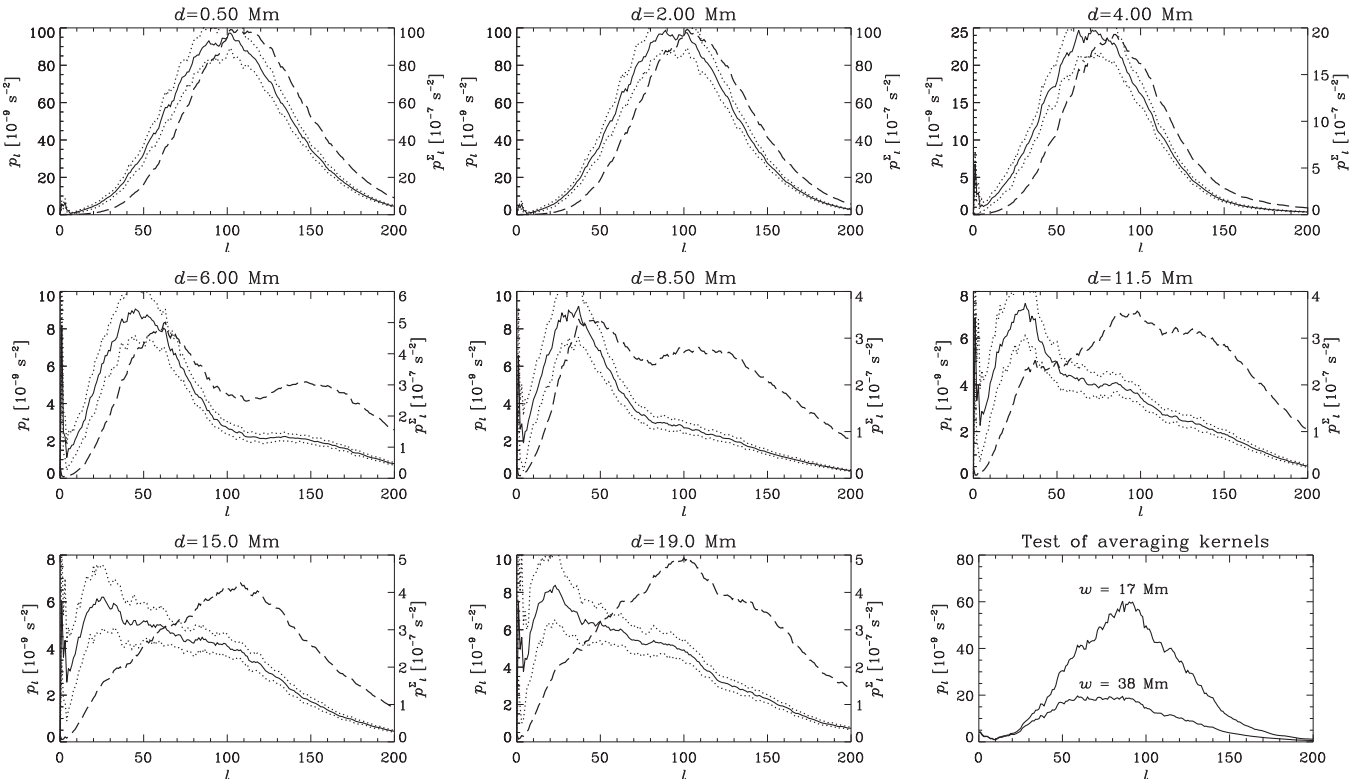

Figure 7. Solid curves (in all panels but the last one): the l-variation of the power p_l, based on the above-displayed spectra for different depths (the low-activity period; Figure 5); the dotted curves indicate the standard deviation of p_l from its running average, while the dashed curves indicate the total power, p_l^{Σ}. The depth values are indicated at the top of each panel. The bottom right panel shows the p_l curves obtained for a velocity divergence field at $d = 0.5$ Mm, averaged with Gaussians corresponding to the helioseismic averaging kernels of two different widths, w.

We have to make an important remark in the context of interpreting our results. Zhao et al. (2012a) noted a systematic center-to-limb variation in the measured helioseismic travel times, which must be taken into account in determinations of the meridional velocities in the convection zone. They suggested a procedure for removing this systematic variation, which was subsequently applied by Gizon et al. (2020) and others in their analyses. To assess the possible effects of the systematic center-to-limb variation in the measured quantities on the results of our analysis, we have additionally calculated the m-averaged power spectra, choosing sectors 90° wide in longitude, and repeated by 90°, 180°, and 270° rotations, so as to obtain fields covering the complete longitudinal angle. The sectors were specified to occupy either a (−45°, +45°) or a (−60°, +30°) Stonyhurst longitude range. The computations were done for both high-activity (from 2013 December 21 to 2014 February 4) and low-activity (from 2019 December 21 to 2020 February 4) times. We found that although such source data modifications slightly increase the amplitudes of the spectra (enhancing the "coherence" of the data: the same field is, in this case, repeated four rather than three times in the compound 360° field, thus contributing to the spectrum with a greater weight), they do not significantly modify the shape of the l-averaged and l-summed spectra (Figure 8). In particular, they leave the spectral peak positions unchanged. Thus, the center-to-limb variations do not affect our conclusions.

3.3. Time Variation. The Effect of Magnetic Fields

The power spectra under consideration experience moderate variations over the course of the solar activity cycle. A careful comparison of Figures 5 and 6 reveals some subtle differences. At shallow layers, $d = 0.5$ and 2 Mm, the maximum spectral power, p_{lm}, is somewhat higher during the low-activity period, while the opposite can be noted for the deeper layers. At all depths, especially in the shallow layers, the spectrum is slightly broader in l at the time of low activity.

Although the shape of the spectrum changes very little over the solar activity cycle, variations in the spectrum amplitude or in the total power of the flow, $p_{\rm tot}$, defined by Equation (8), are more pronounced. These variations are shown by the solid black curves in the left column of Figure 9 for all d values, along with the monthly average sunspot number. Visually, these two quantities appear to vary nearly in antiphase at the upper levels, $d = 0.5$ and 2 Mm; to vary nearly in phase at the intermediate levels, $d = 4$–8.5 Mm (where a notable oscillation with a half-year period, 0.063 μHz, contaminates the $p_{\rm tot}$ variation); and to have no definite correlation with the activity level at the bottom levels, $d \geqslant 11.5$ Mm. The half-year oscillation seems to stem from the variation of the inclination of the Sun's rotational axis to the line of sight. To remove this oscillation and isolate the physically conditioned $p_{\rm tot}$ variations on timescales of the order of the activity cycle, we apply a Fourier low-pass filtering procedure.

Specifically, we calculate the fast Fourier transform of $p_{\rm tot}$ as a function of time, filter the resultant spectrum, multiplying it by an appropriate filtering function, $H(\nu)$, where ν is the frequency, and perform the inverse Fourier transform of the filtered spectrum. We use two filters. The first one is an ideal filter:

$$H(\nu) = \begin{cases} 1 & \text{if } \nu \leqslant \nu_{\rm H}, \\ 0 & \text{otherwise}, \end{cases}$$

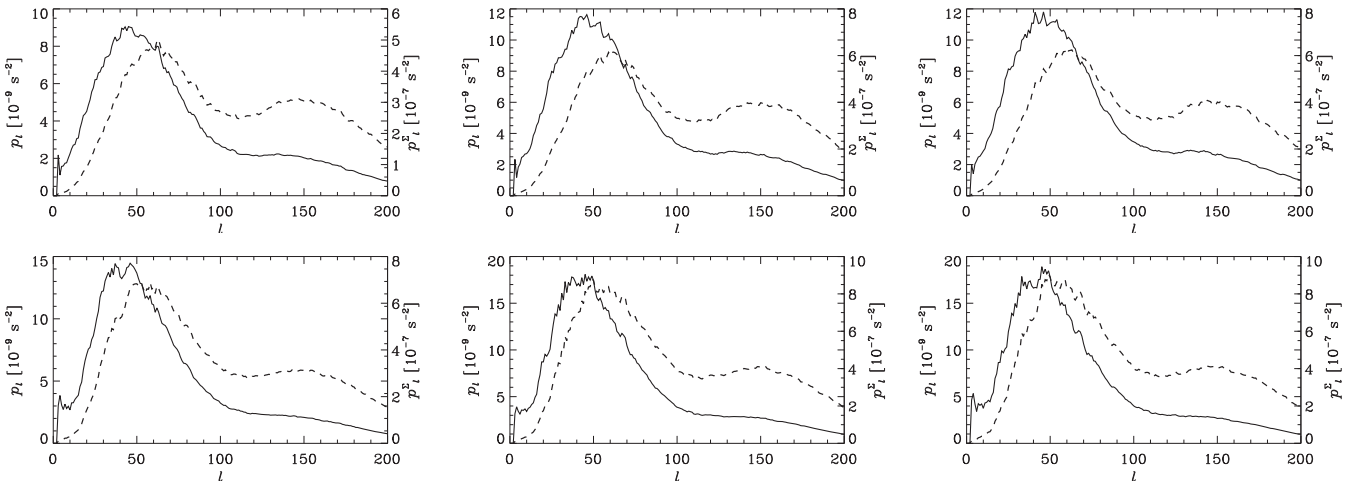

Figure 8. The effect of narrowing the source field sector. The l-averaged (solid curves) and l-summed (dashed curves) spectra are shown for divergence fields at $d = 6$ Mm, differently chosen for spherical harmonic transform: triplicate 120° wide fields (left); quadruplicate 90° wide fields of the (−45°, +45°) sector (middle); quadruplicate 90° wide field of the (−60°, +30°) sector (right). Top: the low-activity period, from 2019 December 21 to 2020 February 4; bottom: the high-activity period, from 2013 December 21 to 2014 February 4.

and the second one is a Butterworth low-pass filter:

$$H(\nu) = \frac{1}{1 + (\nu/\nu_H)^{2n}},$$

where ν_H is the filter cutoff frequency; we assume $\nu_H = 0.05$ μHz and $n = 4$. The algorithms of the discrete Fourier transform yield spectra that are periodic in frequency. The second half of the period corresponds to the negative frequencies decreasing in their absolute magnitude from a maximum (typically put equal to the Nyquist frequency in signal processing) to zero. Accordingly, we extend the filtering function to the second half of the spectra.

The time dependences of $p_{\rm tot}$ obtained using the Butterworth filtering are shown in the right column of Figure 9. We can see that not only does the correlation between the sunspot number and the total power become more pronounced—especially at the medium depths, $d = 4$–8.5 Mm—but this correlation also emerges even at the lowest levels, $d = 11.5$–19 Mm, where it was not notable without filtering. To quantify the possible solar activity dependence of the convection flow energy, we calculate, for each depth, the coefficient of correlation between the convection power and the sunspot number. As can be seen from the black curves in Figure 10, both the anticorrelation at $d = 2$ Mm and the positive correlation at $d = 6$ Mm are especially high for filtered variations, and do not significantly depend on the choice of filter. The two temporal variations are best correlated if the Butterworth filter is used—in this case, the correlation coefficient is −0.901 at $d = 2$ Mm, 0.925 at $d = 6$ Mm, 0.695 at $d = 11.5$ Mm, and 0.324 at $d = 19$ Mm. The depression seen in the unfiltered variation near $d = 8.5$ Mm can be attributed to the enhancement of the half-year oscillation with d, which disappears if a filtering procedure is applied.

A considerable contribution to the cycle dependence of $p_{\rm tot}$ can be made by the magnetic field affecting the time–distance measurements (see, e.g., Liang & Chou 2015). To assess this effect, we additionally performed our analysis for the divergence field, where the actual values in the areas with the radial magnetic field, B, that exceed 200 G are replaced with the mean divergence value over the remaining area. To be brief, we refer to such specially prepared fields as "masked." The field mask is defined as follows:

$$M(\theta, \varphi) = \begin{cases} 0 & \text{if } B(\theta, \varphi) > 200 \text{ G}, \\ 1 & \text{otherwise.} \end{cases} \quad (10)$$

The cycle variations of the total power, $p_{\rm tot}$, of the masked fields, both unfiltered and Butterworth-filtered, are shown in Figure 9 by the dashed curves. The depth variation of the correlation between this power and the sunspot number is plotted with the red curves in Figure 10. It can be seen that although the replacement of the original fields with masked ones has some effect on the amplitude of the power variation, it does not change our conclusions about the anticorrelation of the power with the sunspot number in the upper layers of the convection zone, nor the direct correlation between these two quantities in the deeper layers.

As mentioned at the end of Section 3.2, the spectra of the fields differently constructed for the whole 360° wide longitudinal interval differ insignificantly, only in the spectrum amplitudes, without affecting the spectrum shapes and the positions of the peaks. These differences do not change our findings. Similarly, the variation of the spectra during the solar activity cycle is not sensitive to the procedure of constructing the whole field from the sectors with measured source data. Therefore, our inferences concerning the correlation of the integrated power of convection with the solar activity level remain valid.

4. Conclusion and Discussion

We have analyzed the running average (with a 45 day window) spatial spectra of the horizontal velocity divergence field at depths in the solar convection zone ranging from 0 to 19 Mm. Our spectral analysis of the unsmoothed fields with angular degrees $l \leqslant l_{\rm max} = 1000$ taken into account made it possible to separate the convection signal from the realization noise, with l values exceeding those of 5 minute acoustic waves having their inner turning point at the given d. The spectra definitely reveal flow harmonics with supergranular scales at depths above $d \sim 11.5$ Mm. At depths of $d \gtrsim 6$ Mm, harmonics with giant-cell scales are prominent.

We have made additional computations to assess the possible role of the center-to-limb variations in the measured

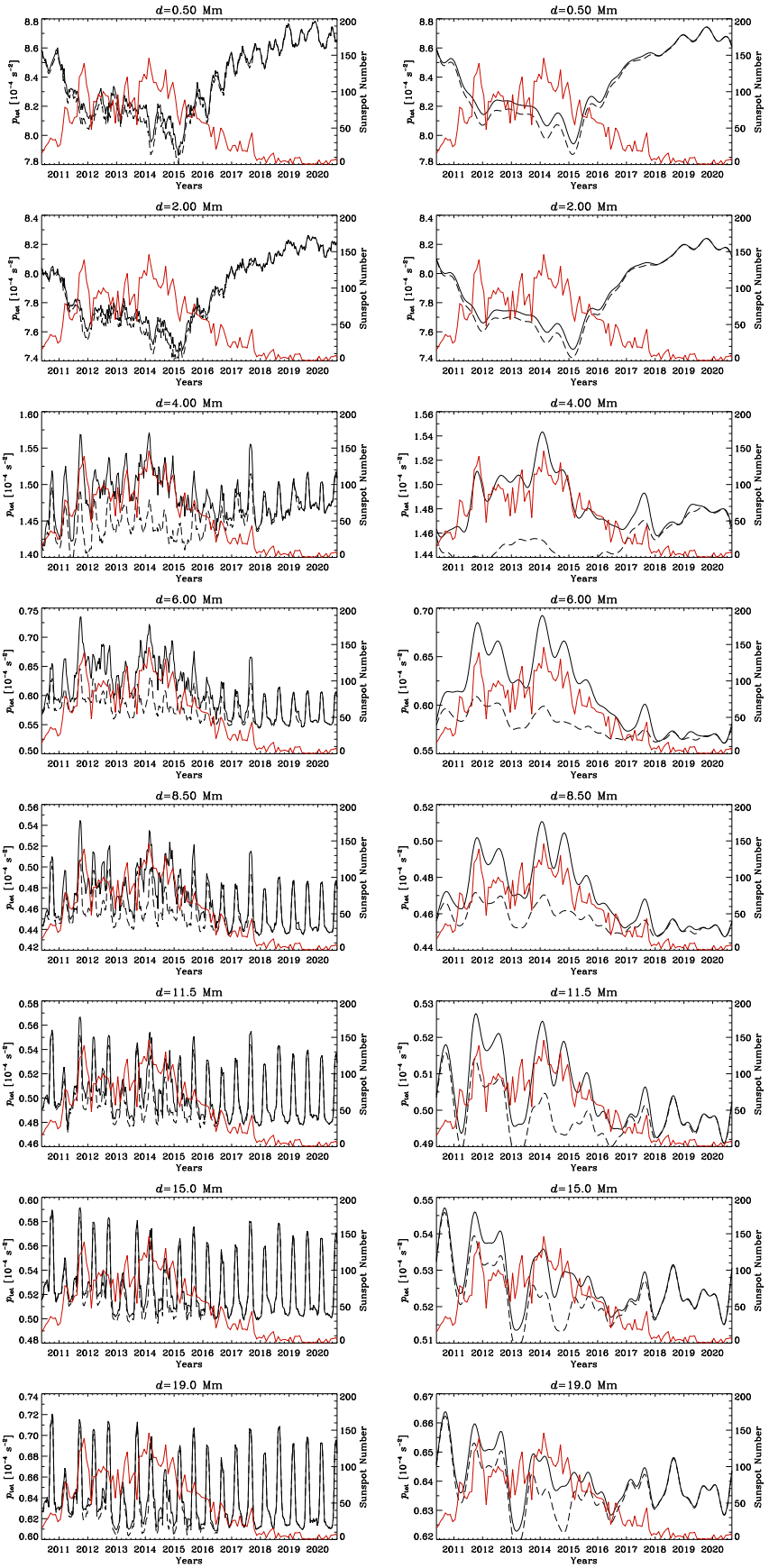

Figure 9. Time variations of the total power of all the harmonics of the unmasked fields (solid curves) and masked fields (dashed curves) for all the depths considered (indicated at the top of each panel). Left: unfiltered; right: filtered by applying the Butterworth filter, with $f_{\rm H} = 14$, $n = 4$. The red curve in each panel represents the monthly average sunspot number.

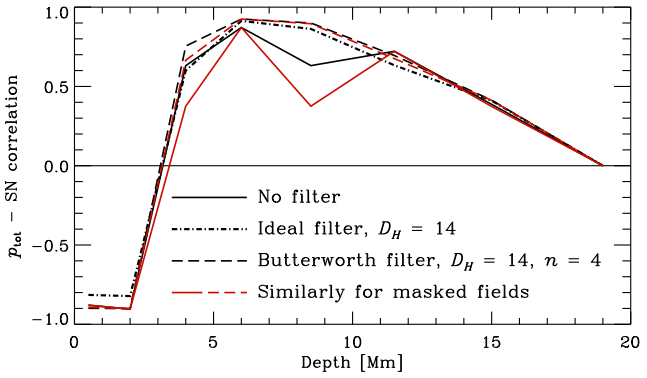

Figure 10. The correlation between the solar cycle variations of the total power of all the flow harmonics and the monthly average sunspot number for unmasked (black curves) and masked (red curves) velocity divergence fields.

helioseismic travel times and found that the inferences of our study are not sensitive to these variations.

The spectral analysis of the divergence fields smoothed with a 17.5 Mm wide window and $l_{\max} = 200$ indicates that the range of flow scales is fairly wide in shallow layers. As the depth increases, this range narrows, and the main peak shifts into the long-wavelength region. While the shortest length scales of the most energetic harmonics in the upper layers correspond to supergranular scales, ∼30 Mm, the largest scales in the deepest layers are about 300 Mm, which is a giant-cell scale. The large-scale components are not clearly noticeable in the top layers, because of the presence of the strong supergranulation component, but their power is of the same order of magnitude as in the deep layers. Such behavior can naturally be interpreted in terms of a superposition of differently scaled flows localized in different depth intervals within the convection zone. In addition, there is some tendency toward the emergence of meridionally elongated (banana-shaped) convection structures in the deeper layers.

We have also considered the time variation of the integrated spectral power of the flow at different levels with the solar activity cycle. To remove the half-year oscillation with a frequency of 0.063 μHz, attributed to the variations in the inclination of the solar rotational axis to the line of sight, we applied a spectral filtering procedure with an ideal and a Butterworth low-pass filter. The results show that the time variation of the total power is anticorrelated with the sunspot number in the shallow layers, $d \lesssim 2$ Mm, and positively correlated at larger depths, $d \gtrsim 4$ Mm. To gain an idea of the possible effects of magnetic fields on the results of time–distance measurements, we additionally performed our spectral analysis replacing the actual divergence values in the areas where the radial magnetic field exceeds 200 G with the mean divergence value over the remaining area. Such masking of the magnetic field regions affects the amplitude of the power variation, but does not change our conclusion about the correlation between the sunspot number and the integrated power of the flow.

The detected relationship between the solar activity and the convective velocity power at different depths can be interpreted in terms of the depth redistribution of the convective flow energy due to the action of magnetic fields. In particular, the large-scale converging flows around active regions, discovered by the ring-diagram (Haber et al. 2004) and time–distance techniques (Zhao & Kosovichev 2004) in the subsurface layers, may affect the convection spectra. In addition, it is possible that mesoscale convective motions associated with the formation of magnetic field structures in the near-photospheric layers interact with larger-scale flows. This important issue calls for further investigation.

We are grateful to G. Guerrero and A. M. Stejko for providing the data of their numerical simulations. The helioseismological data are obtained from the SDO Joint Science Operations Center, courtesy of the NASA/SDO and HMI science teams. We also used sunspot number data from the World Data Center for the sunspot index, and Long-term Solar Observations (WDC-SILSO), Royal Observatory of Belgium, Brussels. The work is partially supported by NASA grants NNX14AB70G, 80NSSC20K1320, and 80NSSC20K0602.

ORCID iDs

Alexander V. Getling https://orcid.org/0000-0002-1766-2620
Alexander G. Kosovichev https://orcid.org/0000-0003-0364-4883

References

Abramenko, V. I., Yurchyshyn, V. B., Goode, P. R., Kitiashvili, I. N., & Kosovichev, A. G. 2012, ApJL, 756, L27
Ballot, J., Roudier, T., Malherbe, J. M., & Frank, Z. 2021, A&A, 652, A103
Beck, J. G., Duvall, T. L., & Scherrer, P. H. 1998, Natur, 394, 653
Bumba, V., Howard, R., & Smith, S. F. 1964, AJ, 69, 535
Busse, F. H. 1970, ApJ, 159, 629
Busse, F. H. 2002, PhFl, 14, 1301
Busse, F. H., & Carrigan, C. R. 1974, JFM, 62, 579
Christensen-Dalsgaard, J., Dappen, W., Ajukov, S. V., et al. 1996, Sci, 272, 1286
Couvidat, S., Gizon, L., Birch, A. C., Larsen, R. M., & Kosovichev, A. G. 2005, ApJS, 158, 217
Couvidat, S., Zhao, J., Birch, A. C., et al. 2012, SoPh, 275, 357
Dahlen, F., & Tromp, J. 1998, Theoretical Global Seismiology (Princeton, NJ: Princeton Univ. Press)
Featherstone, N. A., & Hindman, B. W. 2016, ApJL, 830, L15
Frenkiel, F. N., & Schwarzschild, M. 1952, ApJ, 116, 422
Getling, A. V., & Buchnev, A. A. 2010, ARep, 54, 254
Ghizaru, M., Charbonneau, P., & Smolarkiewicz, P. K. 2010, ApJL, 715, L133
Gizon, L., & Birch, A. C. 2004, ApJ, 614, 472
Gizon, L., Cameron, R. H., Pourabdian, M., et al. 2020, Sci, 368, 1469
Glatzmaier, G. A., & Gilman, P. A. 1981, ApJS, 45, 351
Greer, B. J., Hindman, B. W., Featherstone, N. A., & Toomre, J. 2015, ApJL, 803, L17
Haber, D. A., Hindman, B. W., Toomre, J., & Thompson, M. J. 2004, SoPh, 220, 371
Hart, A. B. 1954, MNRAS, 114, 17
Hathaway, D. H. 1987, SoPh, 108, 1
Hathaway, D. H., Beck, J. G., Bogart, R. S., et al. 2000, SoPh, 193, 299
Hathaway, D. H., Teil, T., Norton, A. A., & Kitiashvili, I. 2015, ApJ, 811, 105
Hathaway, D. H., Upton, L., & Colegrove, O. 2013, Sci, 342, 1217
Herschel, W. 1800, RSPS, 1, 20
Jeans, J. H. 1923, RSPSA, 102, 554
Lefebvre, S., García, R. A., Jiménez-Reyes, S. J., Turck-Chièze, S., & Mathur, S. 2008, A&A, 490, 1143
Leighton, R. B., Noyes, R. W., & Simon, G. W. 1962, ApJ, 135, 474
Liang, Z.-C., & Chou, D.-Y. 2015, ApJ, 805, 165
McIntosh, S. W., Leamon, R. J., Hock, R. A., Rast, M. P., & Ulrich, R. K. 2011, ApJL, 730, L3
Muller, R., Auffret, H., Roudier, T., et al. 1992, Natur, 356, 322
Muller, R., Hanslmeier, A., Utz, D., & Ichimoto, K. 2018, A&A, 616, A87
November, L. J., Toomre, J., Gebbie, K. B., & Simon, G. W. 1981, ApJL, 245, L123
Rieutord, M., Roudier, T., Ludwig, H. G., Nordlund, Å, & Stein, R. 2001, A&A, 377, L14
Rincon, F., & Rieutord, M. 2018, LRSP, 15, 6

Roudier, T., & Reardon, K. 1998, in ASP Conf. Ser. 140, Synoptic Solar Physics, ed. K. S. Balasubramaniam, J. Harvey, & D. Rabin (San Francisco, CA: ASP), 455
Scherrer, P. H., Schou, J., Bush, R. I., et al. 2012, SoPh, 275, 207
Shcheritsa, O. V., Getling, A. V., & Mazhorova, O. S. 2018, PhLA, 382, 639
Simon, G. W., & Weiss, N. O. 1968, ZA, 69, 435
Zhao, J., Couvidat, S., Bogart, R. S., et al. 2012b, SoPh, 275, 375
Zhao, J., & Kosovichev, A. G. 2004, ApJ, 603, 776
Zhao, J., Nagashima, K., Bogart, R. S., Kosovichev, A. G., & Duvall, T. L. J 2012a, ApJL, 749, L5